Estimation of the nearshore bathymetry from high temporal resolution Sentinel-1A C-band SAR data - A case study

Patricia Pereira[a], Paulo Baptista[b,*], Telmo Cunha[c], Paulo A. Silva[d], Soraia Romão[d,e], Virginie Lafon[f]

[a] Departamento de Física, Universidade de Aveiro, Campus de Santiago, 3810-193 Aveiro, Portugal
[b] Departamento de Geociências, Centro de Estudos do Ambiente e do Mar (CESAM), Universidade de Aveiro, Campus de Santiago, 3810-193 Aveiro, Portugal
[c] Departamento de Eletrónica, Telecomunicações e Informática, Instituto de Telecomunicações, Universidade de Aveiro, Campus de Santiago, 3810-193 Aveiro, Portugal
[d] Departamento de Física, Centro de Estudos do Ambiente e do Mar CESAM, Universidade de Aveiro, Campus de Santiago, 3810-193 Aveiro, Portugal
[e] Instituto Dom Luiz (IDL), Faculdade de Ciências da Universidade de Lisboa, Campo Grande, 1749-016 Lisboa, Portugal
[f] I-SEA, Bordeaux TechnoWest, 25 rue Marcel Issartier, 33700 Mérignac, France

ARTICLE INFO

ABSTRACT

The study of the changes in swell properties in the nearshore domain due to interaction with the sea-bottom to infer the bathymetry has deserved some attention in the last few years. Satellite Remote Sensing images, in particular Synthetic Aperture Radar (SAR), have been used to produce a directional wave spectrum by Fast Fourier Transform (FFT), from which the wavelength and wave direction of the ocean surface waves can be retrieved. These wave properties can be directly used in the linear dispersion relation to estimate the water depth.

The present work takes advantages from the very short revisit times of the Sentinel-1A with C-band (5.405 GHz) SAR images with 10 m of spatial resolution to study the repeatability of this methodology for deriving the nearshore sea-bottom morphology, using a case study in the Aveiro region, located in the Portuguese West Coast. This site is exposed to high energetic wave climate of the North Atlantic Ocean. Overall, a set of four images were selected for the analysis.

The robustness of the FFT methodology to calculate the wavelength and wave direction from SAR images was analysed through calculating their standard deviations. The errors of estimating the local bathymetry from these quantities was accessed which allowed to quantify the water depth limits of application of this methodology.

The set of images was used to establish a bathymetric estimation that merges the derived bathymetry of each image. The computed bathymetry was quantitatively compared with the measurements made in 2013 and available at RAIA Observatory. The relative error of the water depth ranges between 6% and 10%, but increases for the higher depths and depends on the accuracy of the computed wavelength at deep-waters. The merged derived bathymetry also provides a better approximation for the measured bathymetry than those derived from the individual images.

1. Introduction

The bathymetric estimation in coastal zones can be considered as one of the most important challenges in oceanography studies such as: (i) research activities in topics related with near-shore geomorphology (Finkl et al., 2005), model calibration and/or validation (Cea and French, 2012), storm, storm surge and tsunami effects (Matsuyama et al., 1999; Goto et al., 2011; Ridente et al., 2014; Ranasinghe et al., 2013) and ecology (Losi et al., 2013); (ii) management applications as harbour security (Grifoll et al., 2011), dredging interventions (Patgaonkar et al., 2007; EL-Hattab, 2014,) and mineral exploration (Basu and Malhotra, 2002); (iii) and economic activities such as fishing (Nishida et al., 2001) and coastal navigation (Dai et al., 2013), among others.

Traditional methods for bathymetric data acquisition in shallow waters (0 to 50 m), with single or multi-beam echo sounder, have the drawbacks of security and cost. This motivates the development of alternative methods of bathymetric estimation. In this aim, several remote sensing techniques have been proposed in the last decades to estimate the sea bottom topography.

Multi or hyperspectral optical satellite or airborne sensors exploit the wavelength dependence of the attenuation of light in the water column to infer water depth from the amount of light reflected from the bottom (Adler-Golden et al., 2005; Sandidge and Holyer, 1998). Several reflectance-based algorithms were developed, which are limited by water transparency (seeing the bottom) and by the variability in the optical properties of both the water column and the reflecting bottom material (e.g., Adler-Golden et al., 2005). In general, in high energetic coasts with suspended sediments the application of these algorithms is limited to water depths between 0 and 6 m.

In deeper places, a series of alternative methods have been developed. The change of wave properties along coasts exposed to swell has deserved some attention in the last few years (Brusch et al., 2011; Lehner et al., 2012; Mishra et al., 2014). Wave refraction is induced by underwater topography. As waves propagate from deeper to shallower water, their wavelength decreases while the wave direction changes. These properties can be used to derive underwater features (Mishra et al., 2014). Brusch et al. (2011) were one of the first to propose the application of the Fast Fourier Transform (FFT) over a single SAR (Synthetic-Aperture Radar) image to produce a directional spectrum where the signature of swell waves is well represented. From the directional spectrum, the wavelength and wave direction can be retrieved and used in the linear dispersion relation to estimate the water depth. The synergy and fusion of optical and SAR data for bathymetric estimation with comparison with in situ echo sounding data was also explored (Pleskachevsky et al., 2011).

The FFT was previously adopted to analyse a sequence of radar images (Young et al., 1985). In fact X-Band radars have been used for many years to image the sea surface (Bell, 1999). Small wind-induced ripples on the sea surface cause Bragg scattering of the incident radar energy, and this scattering is in turn modulated by the surface gravity waves, leading to what is known as 'sea clutter' on a radar screen. The resulting radar images show alternating regions of strong and weak backscatter corresponding to the location of waves (Bell, 1999). The two-dimensional FFT allow define the wavenumber spectra that are inverted to frequency spectra using linear Airy wave theory and knowledge of the water depth. Today, marine radars are often used operationally to measure the spectral quantities of ocean surface waves. They also have shown to be very useful to measure surface winds and currents as well as bathymetry (Horstmann et al., 2015).

Spaceborne synthetic aperture radar (SAR) imaging is particularly suitable for these coastal applications because of its high resolution, global coverage, and daylight and weather independency. Brusch et al. (2011) attempt to establish the applicability of SAR data obtained from the commercial available TerraSAR-X (TSX) data. According with Li et al. (2010) TSX (with a mean orbit altitude of 514.8 km) has a lower R/V value (ratio of satellite slant range R to platform velocity V), when compared to conventional SEASAT SAR (800 km), ERS-1 SAT (782–785 km) and ENVISAT ASAR (800 km). Due to this, the imaging effects of SAR for ocean wave are significantly reduced in TSX data compared with the conventional SARs. More recently, Mishra et al. (2014) evaluated the applicability of SAR data obtained also from the RISAT-1 C-band commercial products (with a mean orbit altitude of 536 km). The Sentinel-1A mission launched in 2014, followed by the second (Sentinel-1B) in 2016, although with a higher orbit height (693 km), when compared with TSX and RISAT-1, opened new opportunities due to the freely available SAR products. The Sentinel-1 missions include C-band imaging operating in four exclusive imaging modes with different resolutions (reaching less than 5 m) and coverage (up to 400 km). They provide dual polarisation capability, very short revisit times and rapid product delivery. Wiehle and Pleskachevsky (2018) follow a previous algorithm developed by Pleskachevsky et al. (2011) to derive the bathymetry from Sentinel-1.

The nearshore bathymetry consists of a variety of morphologic patterns that span a broad range of spatial and temporal scales. According to Plant et al. (2002), nearshore sandbars may exhibit significant response within an approximately seasonal cycle (e.g. Winant et al., 1975; Lippmann and Holman, 1990) and even over decades (e.g. Birkemeier, 1985; Lippmann et al., 1993; Ruessink and Kroon, 1994; Plant et al., 1999). Attending to the very short revisit time of Sentinel-1 (weekly) and considering that the sea bottom morphologic features with the largest spatial scale as nearshore sandbars have the slowest response times, in the scope of the most common morphologies present in the nearshore region (e.g. beach cusps at shoreline and ripples), it seems suitable to explore the high temporal resolution of the Sentinel-1 products and their repeatability to estimate the nearshore bathymetry.

In this work SAR products obtained from the freely available Sentinel-1 mission are explored through the FFT methodology to estimate the nearshore bathymetry in a coastal stretch located at the West Portuguese coast, which is exposed to high energetic North Atlantic waves. This work examines some aspects less explored in the previous Brusch et al. (2011) and Mishra et al. (2014) papers concerning the internal consistency of the adopted methodology to retrieve the nearshore bathymetry, namely: (i) the sensitivity of the waves characteristics estimation to input parameters; (ii) how the repeatability of images can be used to improve the bathymetric results and (iii) the limitations and uncertainties associated with this determination.

2. Study site

The sector located between the Aveiro lagoon mouth (Barra) and Praia de Mira beach along the Portuguese west coast was selected for this study (Fig. 1). It is about 20 km long and morphologically is characterized by a sandy barrier with a linear configuration extending in a NNE-SSW direction exposed to the Atlantic Ocean waves. This sand barrier is only interrupted by coastal engineering structures (Aveiro harbour jetties at Barra), groin fields (Costa Nova urban front and from Vagueira to Praia de Mira beach) and seawalls (Costa Nova and Vagueira urban fronts).

The continental shelf adjacent the shore is about 45 km width. The slope of the shelf is smooth. It is covered by non-consolidated sediments. According to Ferreira (1993), the sea bottom displays morphological features imposed by oceanographic forcing. The nearshore domain is characterized by an inner longshore sand bar. It is observed at a distance of about 300 m offshore the sub-aerial beach and is 0.5 to 1 m high and 80 to 120 m wide. An outer bar is located about 600 m offshore the sub-aerial beach with an orientation parallel to the shoreline. The continental prism is situated between the outer bar and the edge of the continental platform, where the depths are of about 10 m, and 40 m, respectively.

The Portuguese west coast is a very energetic coast exposed to waves far-generated in the Atlantic Ocean. The predominant waves come from WNW and NNW (79%) and have a mean significant wave height of 2–2.5 m and a peak period of 9–11 s (Andrade and Freitas, 2002). According to Vitorino et al. (2002), from June to September, significant wave heights and mean periods are consistently less than 3 m and 8 s. During winter and transition periods, the mean significant wave heights and periods exceed 3 m (most frequent values of 3–4 m) and 8 s (most frequent mean periods of 8–9 s), with frequent storms defined by a mean significant wave height beyond 5 m (often exceeding 7 m) and mean wave periods of approximately 13 s, which can reach 18 s (maximum peak periods). These wave regimes are compatible with the swell conditions and the existence of the outer and inner bars in the nearshore domain contribute to changes of the physical wave characteristics, through the refraction of incident waves. This coastal area has a mesotidal range (mean 2.2 m) with semi-diurnal tides.
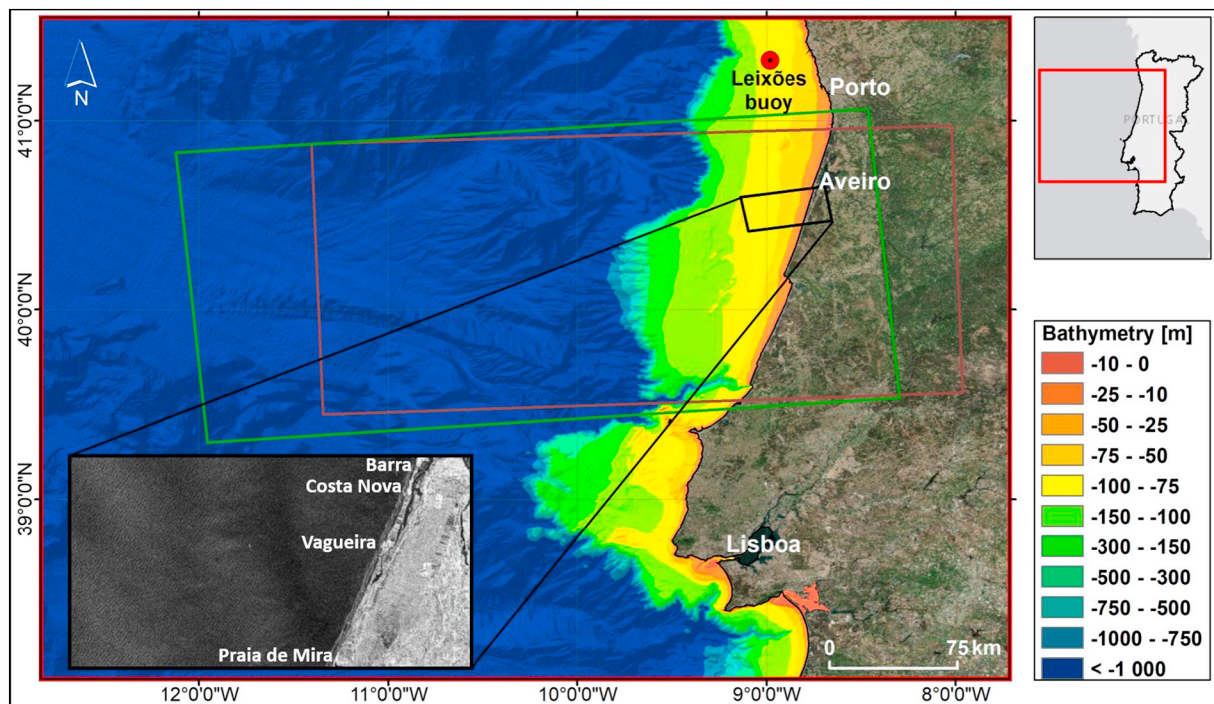
Fig. 1. Map of study area with the location of the Leixões buoy and the Sentinel-1A images (green and red rectangles). The sub-image (black rectangle) between Barra and Praia de Mira represents the coastline that isolates an inner lagoon. (For interpretation of the references to colour in this figure legend, the reader is referred to the web version of this article.)

3. Methodology

3.1. Sensor and data extraction

In this work Sentinel-1A (launched in 2014, with C-band (5.405 GHz)) SAR images have been used to retrieve the bathymetry of the study site. The Sentinel mission, included in the European System of Earth Monitoring Copernicus, operates in four modes of data acquisition, namely *Stripmap* (SM), *Interferometric Wide swath* (IW), *Extra-Wide swath* (EW) and *Wave* (WV) modes.

From the available Sentinel modes of data acquisition, the *Interferometric Wide swath* (IW) with level 1 High Resolution (HR) and Ground Range Detected (GRD) product was considered in this work [resolution = 20 × 22 m (range × azimuth), pixel spacing = 10 × 10 m (range × azimuth), and 5 × 1 (number of looks)]. The GRD consist of focused SAR data that have been detected, multi-looked and projected to ground range using an Earth ellipsoid model such as WGS84 (SENTINEL-1 Team, 2013).

The Sentinel data are freely accessible (https://scihub.copernicus.eu/). They are downloaded through SNAP, which is a free available platform of tools provided by the European Space Agency. SNAP allows the image ortho-rectification through ground control points (GCP) and the images overlap.

The original data have pixel spacing of 10 m. The domain of the image in the study area is situated between latitude ranging from 39.7700 N to 40.9800 N and longitude ranging from 9.8951 W to 8.3245 W. For this domain, each image comprises of 210 GCP. All the available Sentinel-1A images acquired from the launch of the sensor up to March 2016 (880 images) were downloaded and selected taken into account two criteria: (i) the presence of visible swell (65 images from the previous ones) and (ii) the elapsed time between successive acquisitions. This last criterion aimed at choosing the image series acquired over the shortest period of time. A set of four images fulfils these criteria (Table 1).

Table 1
Set of images considered in the present study.

Image code	Data acquisition	Time span between images (days)
07c8	30/01/2015	–
178a	07/02/2015	8
19a7	23/02/2015	16
2ece	13/03/2015	18

3.2. Wave characteristics estimation

Once the images were selected, they were processed individually. This procedure is divided into distinct and successive steps which are described next. One satellite image of the sea surface covers a wide area, where the surface waves present distinct characteristics along such area. According to the method presented in Brusch et al. (2011), it is that distinct behaviour that contains the information from which the sea floor morphology can be inferred. Therefore, it was necessary to divide the image in a grid of small regions, to then estimate the wave characteristics for each such region.

In the first step a grid of centre points is defined over the image. These points define the locations in the image where the local (i.e., in the vicinity of each point) estimation of the wave direction and wavelength is carried out. Next, a squared region (here mentioned as image cell) centred in each point of the grid is defined, whose width is specified independently of the grid spacing (in this way, partial superposition between adjacent cells is allowed).

In a second step, and following the strategy initially proposed in Brusch et al. (2011), the two-dimensional FFT is calculated for each defined squared cell, resulting in a two-dimensional frequency-domain representation of the information content of each cell in the image. It should be noted that a proper selection of the width of the cell should be considered, so that the cell contains sufficient information regarding the local wave characteristics (allowing a proper identification of the dominant wavy behaviour in that region), without covering a too vast region (otherwise the waves might already present distinct
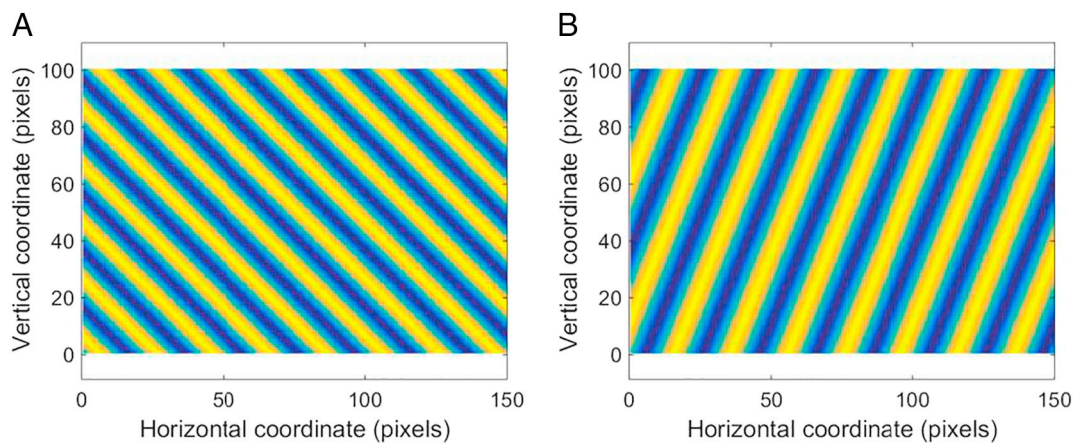
Fig. 2. Two artificially generated images representing a two-dimensional sine wave with linear wave-front.

characteristics through that cell). In summary, the cell dimensions should accommodate several wavelengths (typically on the order of 4 to 10) where the wave characteristics are reasonably constant. As an example, for a wave length of 250 m, the box size should have 1000 to 2500 m or 100–250 px with 10 m image spacing.

The FFT represents the energy that a signal presents distributed with respect to the frequency of each of its components, when considering a decomposition of such signal in sinusoidal components. If a signal presents a sinusoidal-like dominant component, then its Fourier representation will reveal a high peak of energy at the frequency of such component. Therefore, as peaks are easily identifiable features, the FFT is a suitable tool for estimating the characteristics of the dominant sea waves in a specific region. To illustrate this, let us consider the artificially generated images of Fig. 2, consisting of a two-dimensional sinusoidal wave with linear wave-front, assuming a distinct propagation direction in each image, and distinct wavelength.

The application of the two-dimensional FFT to the two images in Fig. 2 results in the frequency-domain representations of Fig. 3 (depicted in magnitude through colour, over the same grid of the images). As can be seen, two sharp peaks appear near the centre of the transformed images (as only one sinusoidal component is present in the images, its energy then appear concentrated at only one frequency point in the transform space – which also requires its complex conjugate term in its symmetric frequency, as the original images correspond to real two-dimensional signals).

Once identified the sharp peaks in the transformed representation, analytical relations are used to estimate the wavelength from the inverse of the distance separating the two peaks, and the wave orientation is estimated from the orientation of the line connecting the two peaks.

As the cell image is discretized in (NxM) pixels (where N is the number of rows of pixels, and M the number of columns), its frequency-domain representation is also discretized in the two-dimensional frequency space (also in (NxM) points). Let dx be the number of columns between the two identified sharp peaks in the frequency-domain representation of the cell image, and dy the respective difference in number of rows. Thus, the wavelength (in number of pixels) of the dominant surface wave of that cell can be estimated through $\lambda = 1/\sqrt{(dx/2M)^2 + (dy/2N)^2}$. The value of the wavelength in meters is then obtained from the former by considering the image spatial resolution. The wave direction is the orientation of the segment connecting the two identified sharp peaks.

Naturally, a real image of the sea surface would not present a so clear sinusoidal wave, which leads to less sharp peaks. However, if dominant swell waves are noticeable in the image, then these would lead to the appearance of the respective peaks in the transformed representation, and the sharpness of such peaks indicates how clear and dominant those wave components are in the image. As an illustration, Fig. 4 presents a region of a satellite image of the sea near the Aveiro coast and its respective transformed representation, where the identification of the dominant peaks (dominant waves) is still quite clear.

After being implemented, this algorithm was tested for several images (both artificially generated – for controlled testing purposes – and real images) and the estimated wave parameters were compared to those expected (from the artificially generated images) and those visually inspected from the real images (where a clear dominant and regular wave was noticed), verifying its correct operation.

The partitioning of the satellite image into cells and the application of the FFT to each of the cells generate the estimate of the wavelength
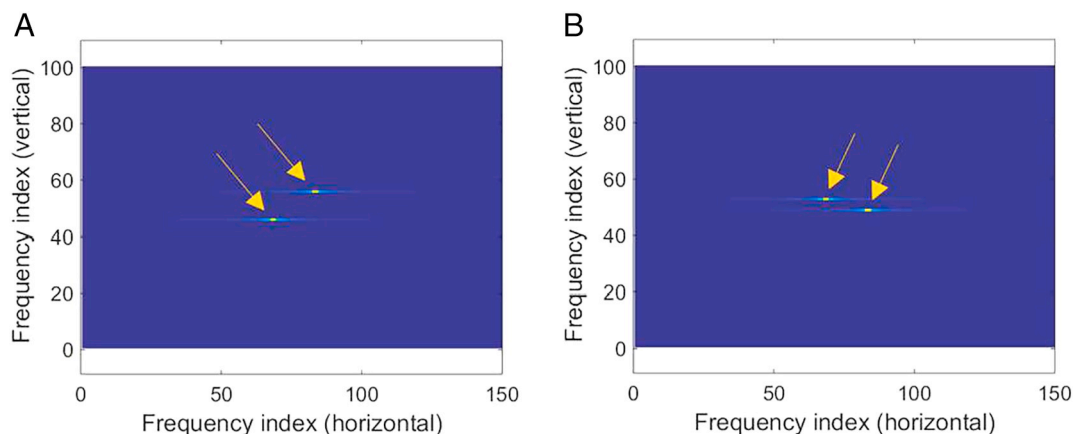

Fig. 3. Representation of the magnitude of the two-dimensional FFT of the two images depicted in Fig. 2.
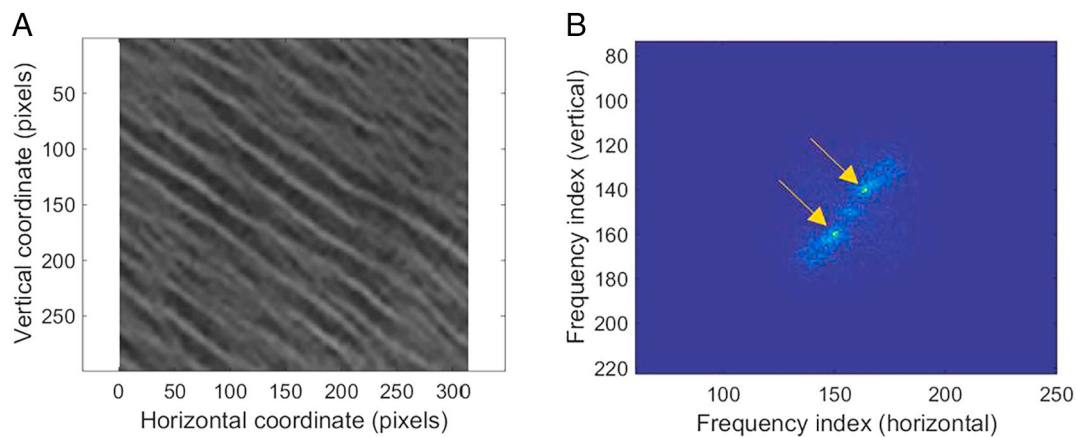
Fig. 4. Region of a satellite image of the sea near the Aveiro coast (A) and the magnitude of the result of the FFT application to it (B).
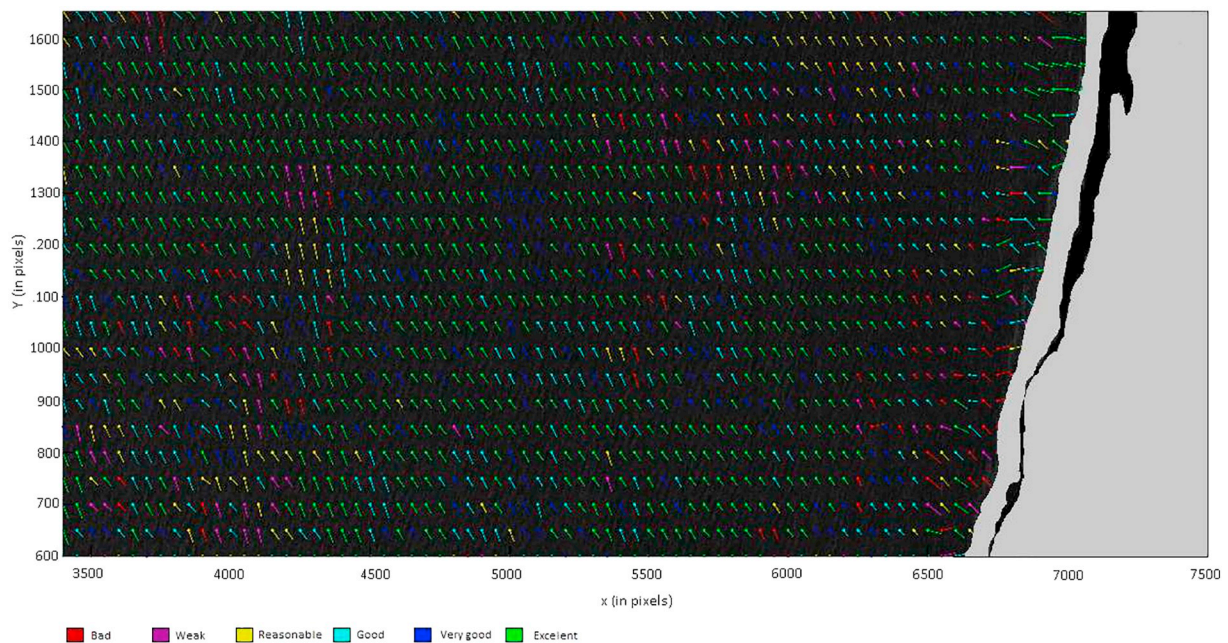

Fig. 5. Illustrative example of the graphical result produced by the wave estimation function, for a satellite image over the Aveiro coast. The length and orientation of the vectors represent, respectively, the wavelength and direction, and the colour provides information on the quality index (red: bad; magenta: weak; yellow: reasonable; cyan: good; blue: very good; green: excellent). Each vector corresponds to one cell of the image, centred in the vector dot. (For interpretation of the references to colour in this figure legend, the reader is referred to the web version of this article.)

and wave direction for all the cells in the image. Moreover, the sharpness of the peaks in the transformed domain provides an indication on the dominance of the identified predominant wave, which is quantified, in each cell, in a scale from 1 to 5 (this is denominated the quality index, where 5 is the highest quality solution). The peak sharpness is evaluated by calculating, in the frequency-domain data, the power contained in frequency circles centred in each identified peaks (these circles have radius d/10, d/4, d/2 and d, where d is half the distance between the two peaks). For a sharp peak, the power contained in these four circles should present a very low variation (as most of the power is within the circle of radius d/10). When the peaks are not so sharp, the power is more distributed along these circles, thus differences are observed on the power contained in each of the four circles. By analysing several image cells, and also distinct images, a (5 level) relation was empirically established between the differences observed in the circle powers and the corresponding inspected quality of the wave identification. This classification is provided to the user, in the end, both in graphical (by means of colours, from red (worst case) to

green (best case)) and numerical form, together with the estimates of the predominant wavelength and wave direction in each cell. Fig. 5 presents an example of the resulting graphical information provided to the user after the automatic processing of a satellite image. A dot is represented at the centre of each cell, from which a line is drawn in the direction of the wave propagation (and the length of this line is proportional to the estimated wavelength). The cells that are located over land are discarded afterwards.

The resulting wavelengths and wave directions are then associated to the coordinates of the centre point of the corresponding cell, in the georeferenced coordinate system provided by the coordinated control points which are attached to the satellite image. This wave information is then ready to be used in the following step, where it is used to estimate the bathymetry of the sea floor in the imaged area.

For the four selected images the best relation between cell size and the typical swell wavelength was evaluated. Based on the quality values determined for each FFT-cell, several sensitivity tests were performed. The cell size was tested for a set of values from 2000 m to 6000 m and
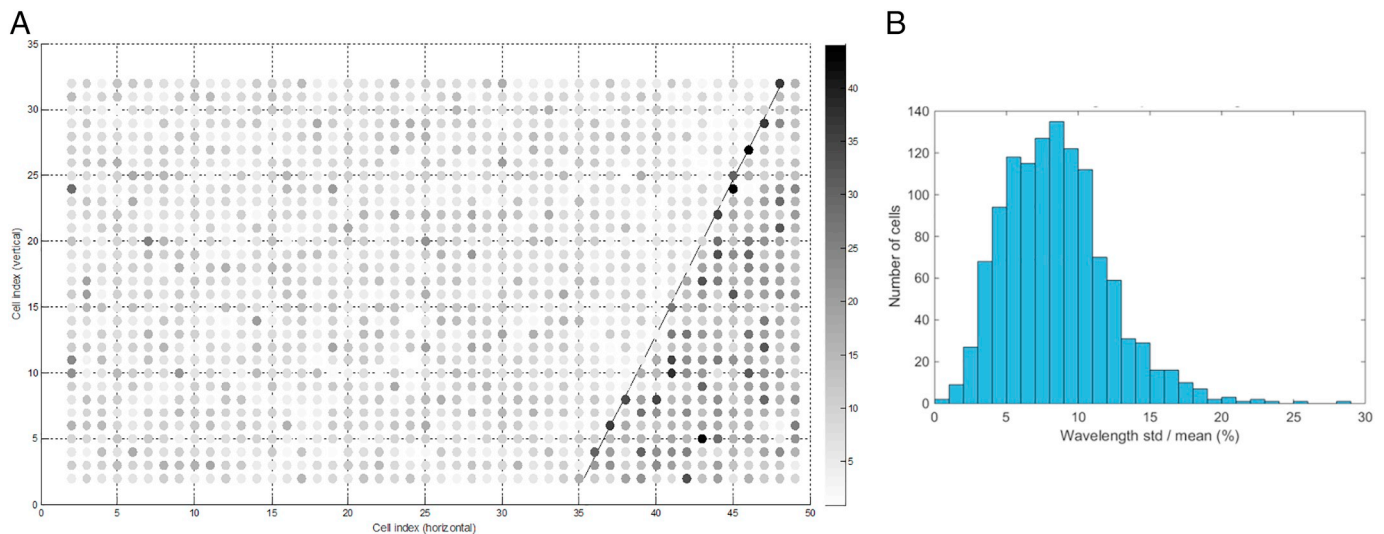
A B

Fig. 6. Analysis of the wavelength variation per cell: A) ratio (in percentage) between the standard deviation and average value of the wavelength estimation in all 441 tests for each cell; B) histogram of the determined ratios. Consecutive cells are spaced by 5 km. The shoreline location is indicated through the line in the figure.

an optimal value of 2500 m (250 pixels) was chosen.

The robustness of this method was also assessed, with the purpose of evaluating if slight modification in the input data could cause relevant differences in the wave characteristics estimation. In this sense, the same satellite image (that of Fig. 5) was processed by this method where, for each processing step, the grid points (i.e., the centre of the cells) were shifted by some pixels with respect to their original position, from one pixel shifts up to the equivalent of 1/3 of the cell width, in all directions. In each iteration, the same shift was applied to all the cells in the images. A total of 441 shifts (iterations) were tested. For each, the resulting cell wavelength and wave direction were calculated and stored, and their variation analysed (for each cell). Fig. 6. A shows the ratio (in percentage) between the standard deviation of the wavelength and the average value of that wavelength, calculated for each cell, considering the results of the 441 tests. Naturally, the cells located in land present a much higher variation. To inspect the wavelength estimation variation, these cells were removed from the analysis and the histogram of variation was determined, which is depicted in Fig. 6.B.

A similar analysis was performed for the estimation of the wave direction in each cell. Fig. 7.A presents the standard deviation (in

degrees) of the wave direction estimates for each cell (considering all the 441 tests in each cell) and Fig. 7.B depicts the respective histogram (without considering the over land cells).

From the results observed in Figs. 6 and 7 it can be observed that the typical (median) standard deviation of the wavelength estimate in a cell is about 7 to 8% of the average wavelength estimate for that cell, and that the typical (median) standard deviation for the wave direction estimate is around 6 to 7°.

3.3. Bathymetric estimation from the linear theory

The linear wave theory, also known as Airy theory, is an analytical solution of the momentum and mass conservation equations that describe the velocity field and pressure along the water column and establishes a relation between the wave celerity, the frequency and the water depth (linear dispersion relation). Airy's equations have asymptotic limits from deep to shallow water as the dynamics of the waves change and become non-dispersive in shallow waters (Phillips, 1977).

The approach considered for determining the sea-bottom depth (h) satisfies the set of values of the wavelength (λ) and the wavelength at
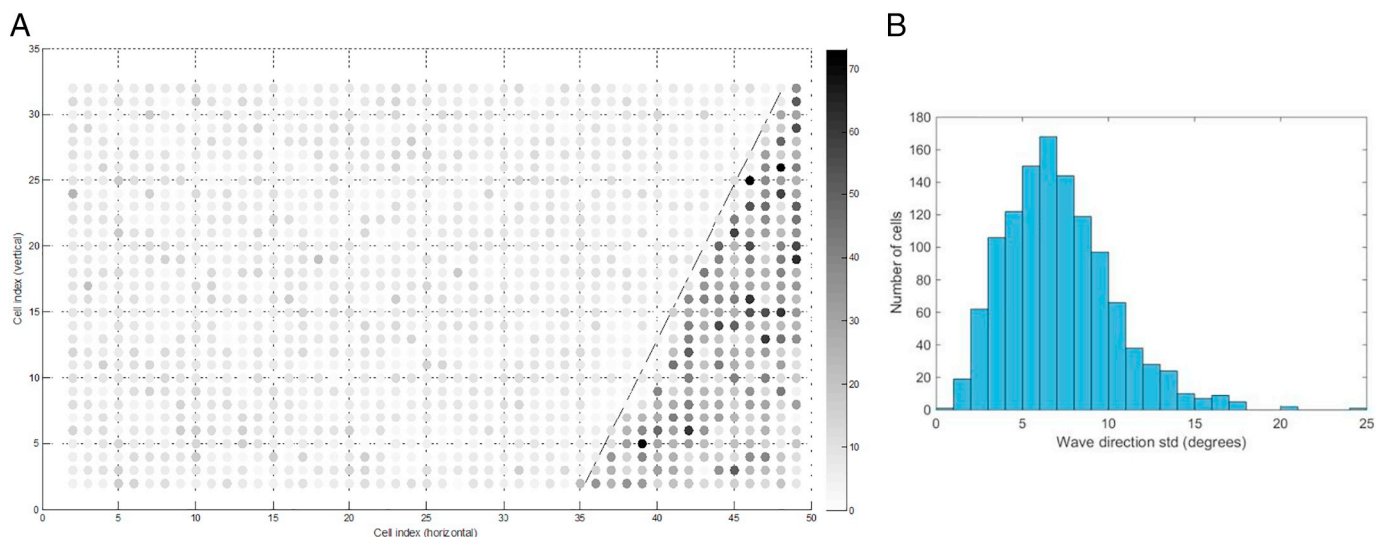
A B

Fig. 7. Analysis of the wave direction in each cell: A) standard deviation (in degrees) of the wave direction estimation in all 441 tests for each cell; B) histogram of the determined wave direction standard deviations. Consecutive cells are spaced by 5 km. The shoreline location is indicated through the line in the figure.

deep water (λ_0) given in the linear dispersion relation:

$$\lambda = \lambda_0 \tanh(kh) \qquad (1)$$

where $\lambda_0 = gT^2/2\pi$, T is the wave period, g is the gravity acceleration, k is the wave number and h is the sea-bottom depth. The effect of a mean current was neglected in Eq. (1).

The bathymetry is computed from:

$$h = \frac{\lambda}{2\pi} \operatorname{atanh}(\lambda/\lambda_0) \qquad (2)$$

The value of λ_0 is determined for each image according to the procedures described in Section 3.2 and considering only the values with a quality index of 5 (best quality) and water depths higher than 200 m, in order to ensure the deep water approximation (water depth larger than half the wavelength). After this procedure the estimated λ_0 and the values of λ computed for each cell as described in Section 3.2 are replaced in the Eq. (2) retrieving the local cell depth. The values of λ_0 and λ are decisive for the accuracy of the calculation of h. The expression to evaluate the relative error of h (Δh) corresponding to an uncertainty in λ_0 or in λ ($\Delta\lambda_0$, $\Delta\lambda$, respectively) was derived from Eq. (2), from indirect measurement error estimation and considering only linear terms in the Taylor expansion. Fig. 8 presents the values of Δh computed at different depths taken as an example an offshore wave period of 8, 12 and 16 s and assuming $\Delta\lambda_0$, $\Delta\lambda$ equal to 5% and 10%. In these calculations the values of λ were computed according to the dispersion relation. The dependency of Δh on $\Delta\lambda_0$ and $\Delta\lambda$ is very similar except for water depths below 10 m. As expected the accuracy of the computed values of h depends on the errors $\Delta\lambda_0$ and $\Delta\lambda$ but it also depends on the wavelength (wave period) of the incoming wave

(increases with λ_0) and on the water depth (increases for shallow waters). The non-linear behaviour of Δh implies that for $\Delta\lambda_0 = 5\%$, a relative error of h smaller than 10% is only attainable for water depths below 15 m, 30 m and 55 m for $T = 8$, 12 and 16 s, respectively, which shows the limits of application of this methodology.

3.4. Two-dimensional low-pass filtering of bathymetric results

The bathymetry estimation has a non-realistic high variability behaviour along space. In order to filter the noise in the computed values of h a two-dimensional low-pass filter was designed to be implemented over the obtained bathymetric results. The applied filter is a continuous bell-shaped filter with flat top that is symmetrical in all directions from the origin of the two-dimensional wave number domain and has two input parameters: the Filter Width is the scalar indicative of the width (in the frequency domain) of the filter; the Filter Sharpness is the scaler indicating how sharp the transition between the pass- and reject-bands is. In Fig. 9 is a representation of the magnitude of one instantiation of this low-pass filter, in the two-dimensional wave number-domain, and in Fig. 10 is an example of its application to a section of the bathymetric result, clearly showing the high wave number components that, before filtering, are disturbing the more natural sea floor morphology, being eliminated after filtering.

Adequate tuning of the filter parameters was performed in order to retain the predominant variation of the sea bottom morphology, filtering out its non-realistic high-frequency variations.
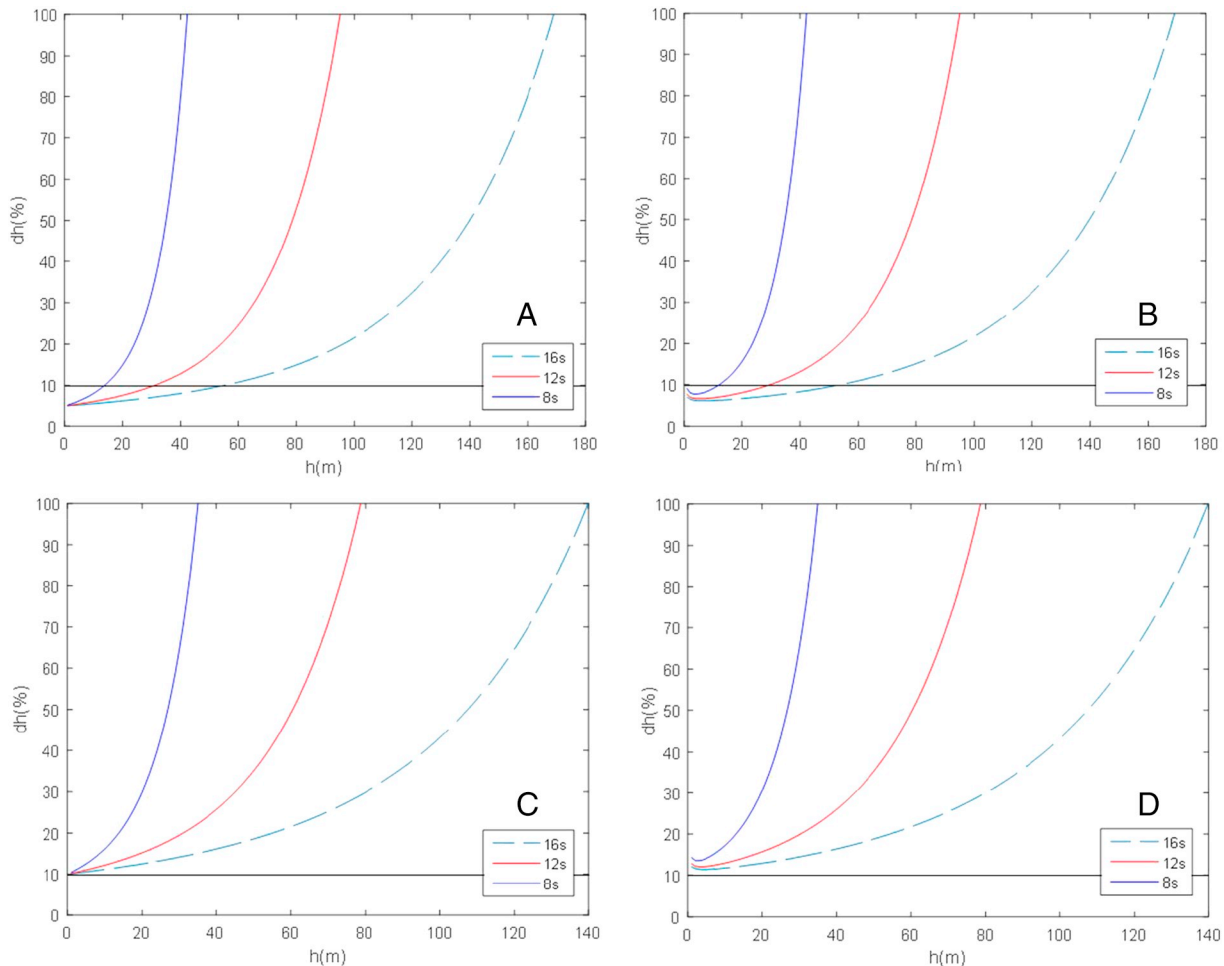

Fig. 8. Relative error of h (Δh) at different depths for offshore wave period of 8, 12 and 16 s and A) $\Delta\lambda 0 = 5\%$, B) $\Delta\lambda = 5\%$, C) $\Delta\lambda 0 = 10\%$ and D) $\Delta\lambda = 10\%$.
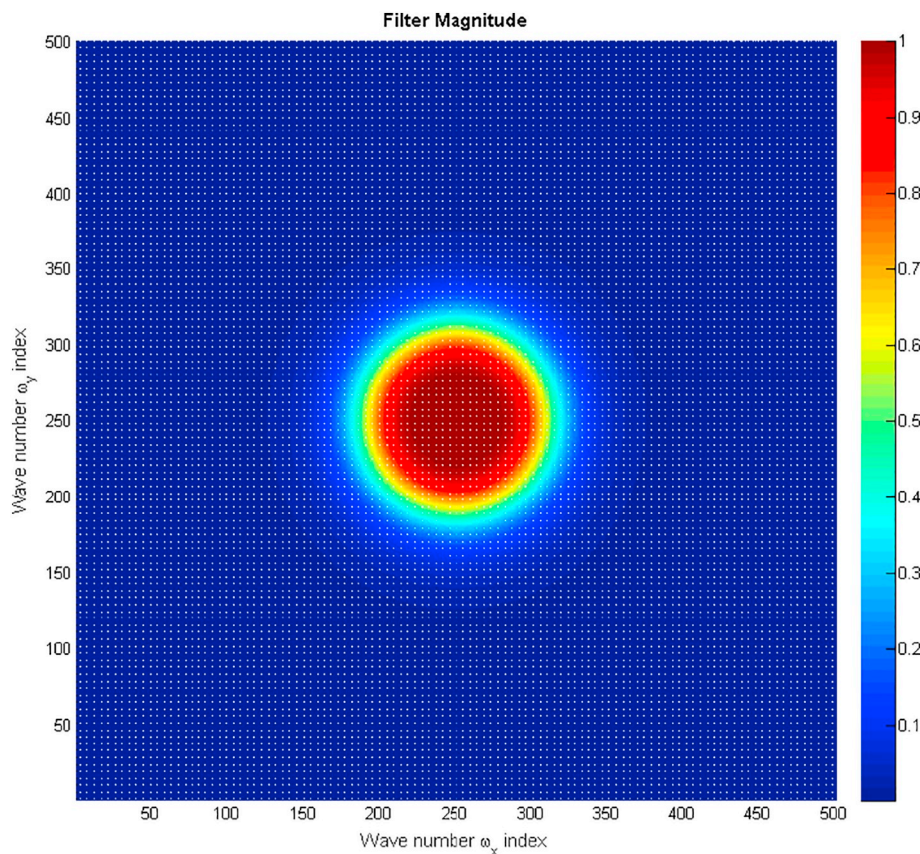
Fig. 9. Magnitude representation of the two-dimensional low-pass filter used to process, at the last stage, the bathymetric results. The centre point of this graph corresponds to the origin of the wave number domain.
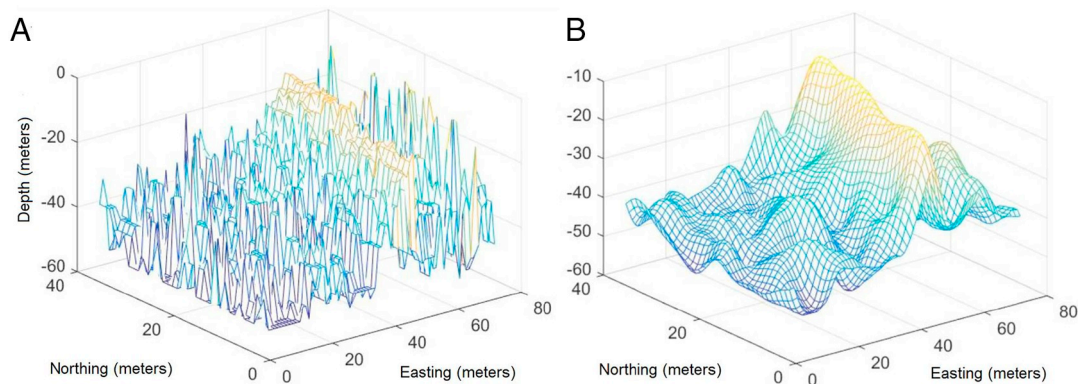

Fig. 10. Example of the bathymetric result of a section of the area under analysis: A) before applying the two-dimensional low-pass filter; B) after the application of the filter.

4. Results

The bathymetry for all the images listed in Table 2 was computed for the coastal sub-images (Fig. 1). The values of λ_0 estimated from the image analysis are presented in Table 2 and compared with the values retrieved from the peak wave period (T_P) observed at the Leixões buoy, located 70 km north of the study site, λ_{0T} (see Fig. 1). The set of values for λ_{0T} were obtained considering the maximum, minimum and mean values of T_P measured during the day of image acquisition and at the time of image acquisition. The results show that there is a good agreement between the λ_0 value computed from the SAR images and those from the wave buoy data when the maximum values of T_P are considered (the relative error ranges between 0.4% (image 07c8) to 13% (image 2ece)).

On the other hand, as the image cells approach the shore, a significant number of land pixels are considered in the FFT computation which imposes an onshore limit on the validity of this method. The computations made for a suitable set of FFT cell dimensions showed increasing errors for water depths below 15 m. Moreover, the uncertainty in the wavelength determination (estimated in about 7 to 8%), and the typical wave periods measured at the buoy (Table 2) limits accurate estimations of the water depth below 30 m, according to Fig. 8. Hence, the application of the present methodology for this study site is expected to give reasonable results for water depths between 15 and 30 m.

Table 2
Wave data measured at Leixões buoy and comparison between the deep-water wavelength computed from the image (λ0) and from the peak period (λ0 T).

Image	Acquisition date and hour	H_s (m)		T_p (seg)	λ_{0T} (m)	λ_0 (m) satellite imagery	λ_0 - λ_{0T} (m)
		Buoy measurements					
07c8	30th Jan	Minimum	4.34	10.50	172	437	265
	2015 06 h42	Mean	4.82	14.25	317		120
		Maximum	5.48	16.70	435		2
		Hour$_{acq}$	4.61	16.70	435		2
178a	17th Feb	Minimum	2.80	13.30	276	306	30
	2015	Mean	3.47	14.05	308		−2
	18 h35	Maximum	4.20	14.30	319		−13
		Hour$_{acq}$	2.97	13.30	276		30
19a7	23th Feb	Minimum	2.47	11.10	192	269	77
	2015	Mean	3.39	11.75	216		53
	06 h42	Maximum	4.27	12.50	244		25
		Hour$_{acq}$	2.84	11.10	192		77
2ece	13th Mar	Minimum	2.05	10.50	172	283	111
	2015	Mean	3.16	12.51	244		39
	18 h35	Maximum	4.33	14.30	319		−36
		Hour$_{acq}$	4.12	13.30	276		7

4.1. Repeatability of the adopted methodology to estimate the bathymetry

A set of nearshore isobaths 5 m spaced from 15 m to 30 m below Mean Sea Level (MSL) were considered. The differences in the water depth computed from each image in relation to a reference image were computed through the algorithm described in Baptista et al. (2011). Image 178a was used as reference taken into account its general linear trend behaviour. The calculations were made both for the unfiltered and filtered isobaths: the low-pass filter smooths the high frequency oscillations for the calculated isobaths but the trends are similar as the unfiltered results. Therefore, in the following analysis only the filtered solutions are presented. Fig. 11 plots the water depth differences computed for the isobaths of 15 m, 20 m, 25 m and 30 m and Table 3 presents a quantitative analysis of the results.

The visual inspection of the calculated isobaths (15, 20, 25 and 30 m) obtained from images 07c8, 19a7 and 2ece, in relation to the reference image 178a, reveals similar trends of alongshore behaviour but no systematic differences between the results. For the 15 m isobath there is a clear deviation between image 19a7 and the other two images results whereas for the isobath of 25 m, images 19a7 and 2ece produced more similar results comparatively to image 07c8. The water depths obtained from images 07c8, 19a7 and 2ece are in most of the cases lower than the water depth predicted by image 178a. Fig. 11 also shows that the differences between the water depths computed from the different images increases from the 15 m to the 30 m isobath: the mean value of the deviation is equal to 1.3 m for the isobath of 15 m, 2.2 m for the isobath of 20 m, 2.5 m for the isobath of 25 m and 3.4 m for the isobath of 30 m. However, the uncertainty in the water depth evaluation is nearly constant and around 10%. Also notice that the standard deviation for image 19a7 is higher than for the other images which can be linked to the higher uncertainty in the λ₀ computation (see Table 3).

4.2. Single- versus ensemble-calculated bathymetry

To evaluate the accuracy of the method, the calculated isobaths from satellite images are compared with the bathymetry provided by the Oceanographic Observatory of the Iberian Margin (RAIA Observatory), in the following denoted by RO bathymetry. This is a 2013 high resolution bathymetry for the North West of Iberian Peninsula (resolution of half a nautical mile), and was obtained from the General Bathymetric Charts of the Oceans (GEBCO) as background field and different measurements and bathymetries (https://www. meteogalicia.gal/web/modelos/threddsIndex.action?request_locale = es). The calculated isobaths were corrected taken into account the

astronomical tidal elevation at Barra (see Fig. 1) at time of image acquisition (−0.70 m, −1.0 m, 1.3 m and 0.51 m to mean seal level for 07c8, 178a, 19a7 and 2ece, respectively) enabling comparison with the bathymetric survey. As an example, the 20 m isobath from RO and that calculated from satellite image 178a are displayed in Fig. 12. The results reveal that the 20 m isobath calculated from image 178a is disposed parallel to the coast, oriented NNE-SSW, and follows the same trend of the RO data.

The relative error of the water depth for images 07c8, 19a7, 2ece and 178a, for the isobaths considered, range between 8% to 17%, 2% to 13%, 17% to 24% and 0% to 6%, respectively. Therefore, the most accurate estimated depths are those obtained with image 178a and the least accurate with the image 2ece. Also there is more variation of the results for the 25 and 30 m isobaths, as the standard deviation increases from 1.4 m (15 m isobath) to 2.9 m (30 m isobath).

An ensemble calculated bathymetry, which averages for each cell the results obtained with the four images, was determined and the results are presented and compared with the ones of the RO bathymetry, denoted as RO isobaths in Fig. 13. The calculated 20 m isobath has a general trend that is close to the RO isobath although it tends to depart eastward from the RO bathymetry. This trend is also observed for the remaining isobaths which suggests the presence of an offset between the two data sources along all the longitudinal extension of the domain. This means that at those locations the estimated bathymetry is deeper than the measured one. On the other hand, the offset is higher for the isobaths of 25 m and 30 m which result in a larger distance between the isobaths.

The statistical analyses of the differences between the ensemble and the RO bathymetries are presented in Table 4. The 20 m isobath shows the best statistical results, while the worst ones appear for the isobath of 30 m. The relative error for the water depth determination ranges between 6% and 10%, which improves the results obtained for the individual images, except for image 178a.

5. Discussion

The application of Fast Fourier Transform (FFT) to produce a directional spectrum of an image for bathymetric estimation in the nearshore regions was proposed some years ago and only a few works have been dedicated to this research topic (Brusch et al., 2011; Pleskachevsky et al., 2011; Lehner et al., 2012; Mishra et al., 2014; Wiehle and Pleskachevsky, 2018). Table 5 compiles the satellite data sources that have been used in some of these works, the main differences in the implemented methodology and the result comparisons with other data sources in the adopted study sites.

The FFT methodology is implemented through a FFT-cell that moves from the open sea by a constant (Mishra et al., 2014) or variable distance imposed by the wavelength (Brusch et al., 2011; Lehner et al., 2012). This procedure is repeated along the tracked wave rays (Brusch et al., 2011; Lehner et al., 2012) or in a constant direction (Mishra et al., 2014) until reach the shoreline. Filters were used previous to the FFT cell implementation as the Kernel filter in Mishra et al. (2014) to resize the image spatial resolution and reduce noise or during FFT-cell implementation for the wave direction (cross sea) filtering and wavelength (wind sea and wind streaks) filtering (Lehner et al., 2012).

This methodology is particularly suited to derive wavelength and wave direction of swell waves, in nearshore regions. In general, it is limited to water depths between the domain in which the swell wave starts to interact with sea bottom (50 m to 30 m) and wave break zone, namely the surf zone (10 to 5 m). These range values are dependent on the study site constraints.

Previously, Brush et al. (2011) used TerraSAR-X data and compared the results in a qualitative way with ETOPO-1 bathymetry and some local bathymetric charts. In Mishra et al. (2014), RISAT-1 SAR data was used for the retrieval of wave field and bathymetry. According to these authors the general trend of the obtained bathymetry from RISAT-1
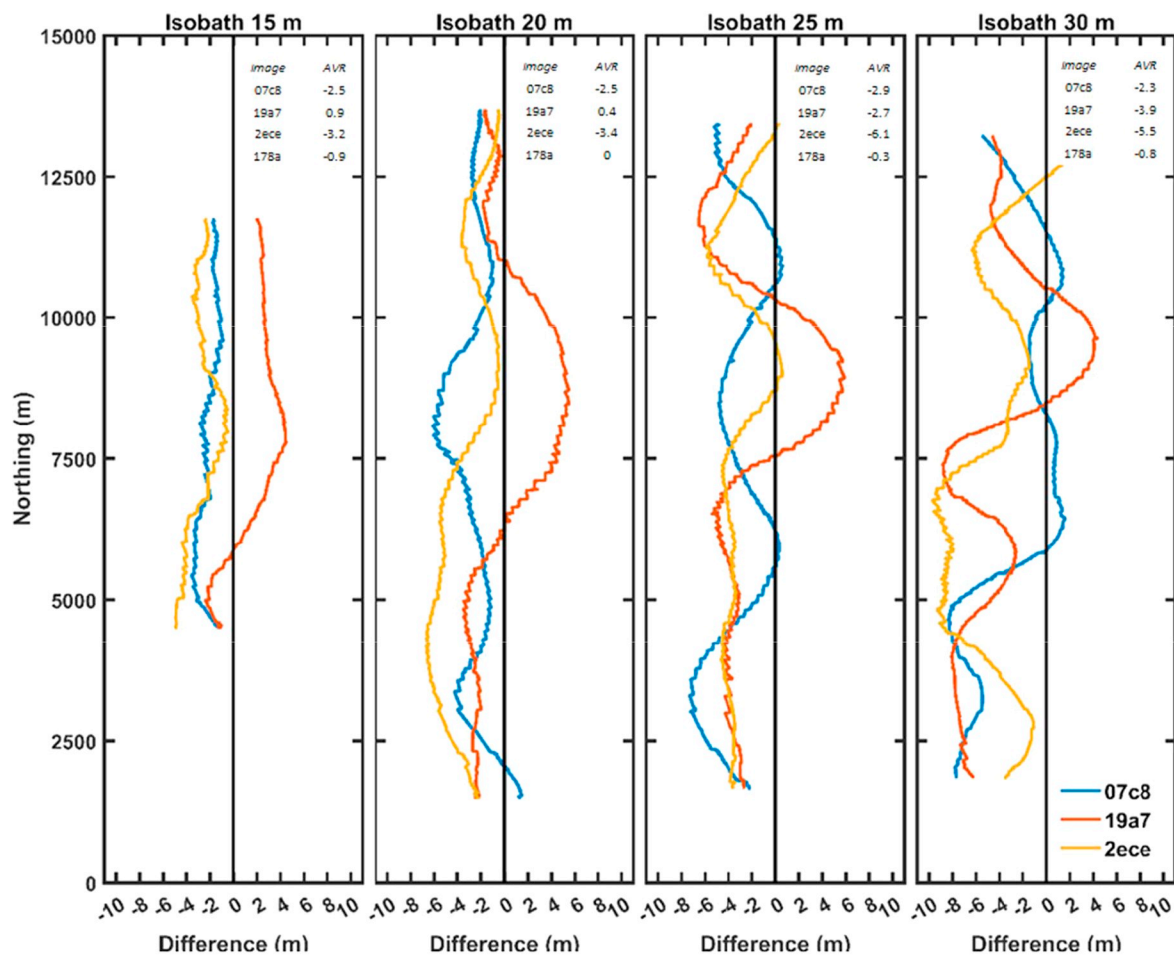
Fig. 11. Differences between water depths computed from the reference image 178a and the images 07c8, 19a7 and 2ece for the isobaths of 15, 20, 25 and 30 m. For each isobath the average value in meters (AVR) is represented.

Table 3
Statistical analysis (minimum, average, maximum and standard deviation) of the differences between the water depth calculated for each image and those from the reference image 178a for the isobaths of 15, 20, 25 and 30 m (in meters).

Isobath	Image	MIN	AVR	MAX	STD
15 m	07c8	−3.5	−2.1	−0.9	0.7
	19a7	−2.4	2.0	4.4	1.9
	2ece	−4.9	−2.7	−0.5	1.2
	Mean		−1.0		1.3
20 m	07c8	−6.1	−2.6	1.5	1.6
	19a7	−3.5	0.2	5.5	2.9
	2ece	−6.7	−3.5	−0.4	2.0
	Mean		−2.0		2.2
25 m	07c8	−7.3	−3.1	0.6	2.3
	19a7	−6.5	−2.1	5.8	3.6
	2ece	−5.9	−3.1	0.6	1.6
	Mean		−2.8		2.5
30 m	07c8	−8.3	−2.4	1.6	3.3
	19a7	−8.8	−3.9	4.3	3.7
	2ece	−9.7	−4.5	2.9	3.2
	Mean		−3.6		3.4

Fig. 12. Calculated isobath of 20 m from the satellite image 178a over the RO bathymetry. The coastline is represented by the grey straight line that isolates the inner lagoon.

SAR data agrees with the available global bathymetric maps (e.g., ETOPO-1 bathymetry toposheets). However, ETOPO-1 gives bathymetry at a very coarse resolution (1 min ~ 2 km), while in Mishra et al. (2014), bathymetry has been obtained at 75 m resolution (FFT-cell shift), and hence, statistical comparisons were not possible. These authors mention that the results qualitatively agree with available
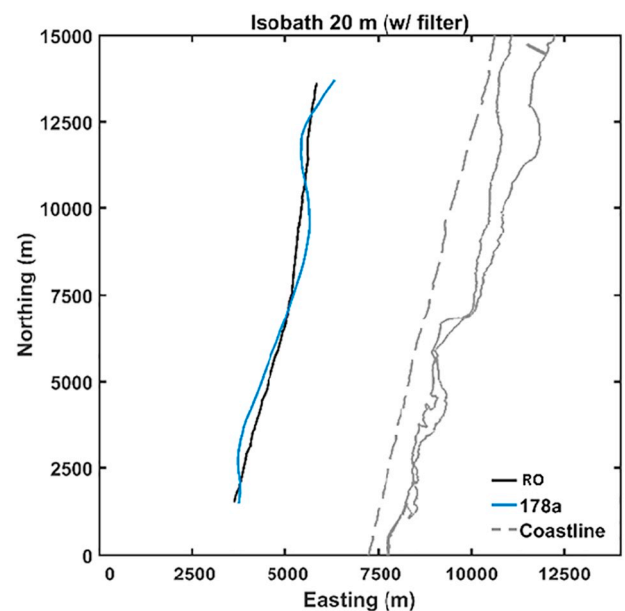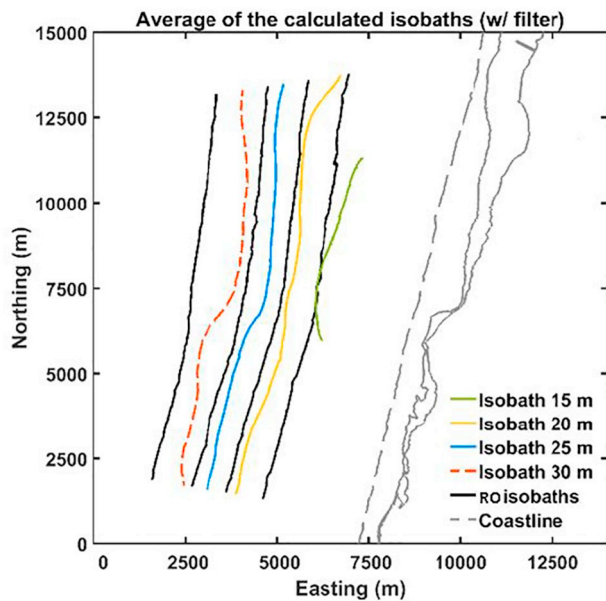
Fig. 13. Isobaths of 15, 20, 25 and 30 m from the ensemble calculated bathymetry over the RO bathymetry. The coastline is represented by the grey straight line that isolates the inner lagoon.

Table 4
Statistical analysis (minimum, average, maximum and standard deviation) of the differences between the averaged images calculated isobaths and RO bathymetry (in meters).

Isobaths	15 m	20 m	25 m	30 m
MIN	− 0.3	0.3	1.0	1.2
AVR	0.9	1.5	1.9	3.0
MAX	2.4	4.1	2.9	4.2
STD	0.7	0.7	0.5	0.8

bathymetric information (ETOPO-1), but a more robust validation is required. As previous mentioned in the Introduction section, while TSX and RISAT-1 have higher resolution acquisition modes and better imaging of the ocean surface due to a comparably low orbit altitude, when compared with Sentinel-1A, the data are only available when previously ordered.

Coastal shores exposed to high energetic regimes in which the frequency of swell waves is high during significant periods of time provide the opportunity to explore the high temporal resolution of the new freely available satellite products, as Sentinel-1A. On the other hand, Sentinel-1A data is fully accessible, which simplifies the retrieval of suitable scenes worldwide. In Wiehle and Pleskachevsky (2018) work both one scene and the average of ten scenes to retrieve depths in West Africa coast were investigated (Sentinel-1A IW mode). An FFT boxsize of 5.12 km was used, where the FFT cells were arranged in a gridded pattern offset by 700 m. Depth estimation results were compared with GEBCO data. The achieved accuracy in Wiehle and Pleskachevsky (2018) is within 15% for one scene while the average of ten scenes reduces the error by 40%. As is stated by these authors GEBCO dataset used for comparison cannot be considered to contain fully accurate bathymetry in this region.

The methodology adopted in the present work intends to investigate the repeatability of Sentinel-1A IW mode in retrieving the sea-bottom morphology. The adopted methodology to retrieve the bathymetry has a 500 m horizontal resolution (FFT-cell shift) for 2500 m cell size, and a two-dimensional low pass filter was used after bathymetric estimation to filter high frequency oscillations in the computed water depths.

The use of a set of four images obtained over a time horizon of a few weeks, assuming that the sea-bottom for depths higher than 10 m has not changed significantly, permits to assess the internal consistency of the method for retrieving the nearshore bathymetry.

The computed bathymetry between 10 and 30 m depth were compared with the measurements available at RAIA Observatory (half a nautical mile resolution) considering both the results of processing a single image and that of the ensemble of images (which represents the average of the results from the four SAR images).

The calculated averaged altimetry oscillations between these four images comparatively with RO bathymetry, were of the order of a few meters (-1.39 to -2.99 m) with standard deviations of the same order (1.35 to 1.78 m) for the 15, 20 and 25 m isobaths. In the case of the 30 m isobath the averaged values are -3.12 and the standard deviation is 2.86 m. The ensemble image slightly improves the results, with altimetry oscillations between 0.92 and 2.96 and standard deviations from 0.53 m and 0.80 m for all the isobaths. Overall the ensemble provides more accurate water depth estimations than the individual images. The relative error of the water depth ranges between 6% and 10%, increasing for the higher depths.

The results show a negative offset for most of the isobaths and images, indicating that the estimated isobaths are displaced in the onshore direction, and there are differences in the accuracy of water depth estimation between them: the most accurate and precise results were obtained with the image 178a. The higher the isobath, the higher is the variation of the results obtained from the different images and the offset. This can be explained from the dependence of the error on the depth (less accurate and higher variation for increasing depths). In fact, the methodology provides estimates for water depths lower than 40 m because of the increasing errors at higher depths. As an example, taking into account the uncertainty in the computation of both λ and λ_0 of about 7 to 8% the corresponding error Δh is smaller than 10% for water depths below 10 m, 30 m and 50 m for wave periods of 8 s, 12 s and 16 s, respectively.

Note that all the images were collected for nearly the same offshore wave direction conditions: the wave direction observed at Leixões Buoy for the date of the 4 images is from NW and WNW. As can be seen in Table 2, the offshore wavelength estimated from image 178a is 306 m and the wave period has a small variation when compared with the other days. This fact suggests that a correct estimation of the offshore wavelength is fundamental for the accuracy of the method.

As described in Section 4.2 the tidal elevation was taken into account on the computations. Lopes (2016) has analysed the residual levels at Barra tide gauge between 1976 and 2013 (see Fig. 1 for the location) and found that storm surge levels recorded ranged between 0.30 and a maximum of 1.09 m with a mean height of 0.43 m. Storm surges heights higher than 1 m have a return period higher than 50 years. Even if we did not take into account the storm surge level in our computations namely for 07c8 image which corresponds to storm conditions, it is not likely that this process justifies the difference between the computed and observed bathymetry.

6. Conclusions

In this work the application of Sentinel-1A with C-band (5.405 GHz) SAR images with 10 m of pixel spacing has been used to retrieve the bathymetry of the Aveiro (NW Portugal) study site. Coasts exposed to high energetic waves provide excellent opportunities to explore swell wave properties to infer bathymetry. The high temporal resolution of the Sentinel-1A and the recurrent swell wave regime observed during 2015 maritime winter (period between October 2015 and March 2016) allow to investigate the repeatability of the FFT methodology in retrieving the nearshore bathymetry considering a set of four high temporal resolution images. The comparative analysis allows to infer averaged depth oscillations between these four images in each considered isobath (15, 20, 25 and 30 m), shown to be on the order of a few meters with associated standard deviations of the same order. The

Table 5

Data compilation from some remote sensing derived coastal bathymetry using the FFT methodology.

Author	Brusch et al., 2011	Lehner et al., 2012	Mishra et al., 2014	Present work
Study site				
Locations	Duck, NC, USA Port Phillip (Australia)	Duck, NC, USA Port Phillip (Australia) Rottnest Island (Australia) Helgoland Island (Australia)	Mumbay, India	Aveiro, Portugal
Satellite SAR product				
Sensor	TerraSAR-X	TerraSAR-X	RISAT-1 SAR	SENTINEL 1 A
Spatial resolution	3 m	3 m	3 m (resized to 15 m)	10 m
FFT implementation				
FFT cell size		1000×1000 pixel	128×128 pixel	250×250 pixel
FFT cell shift	Variable: 1 wavelength (80–300 m)	Variable: 1 wavelength (80–300 m)	Constant: 5 pixel (75 m)	Constant: 50 pixel (500 m)
Implementation	Wave ray tracking	Wave ray tracking	Constant direction	Constant direction
Range of application (investigated depth)	5 m to 40 m (below MSL)	10 m to 50 m (below MSL)	7.5 m to 30 m (below MSL)	15 m to 30 m (below MSL)
Filter implementation				
Type	n/a	Not indicated	Kernel filter	Bi-dimensional low-pass filter to bathymetric results
Phase of implementation	n/a	Filtering wavelenght and wave direction in FFT cell (wind streaks and wind sea patterns filtered)	Previous FFT cell implementation to resize image	After bathymetric estimation to filter non-realistic high variability behaviours
Comparison with other data sources				
Bathymetric sources	ETOPO-1 US Coastal Relief Model British Admiralty sea Chart (qualitative analysis)	n/a	ETOPO-1 (qualitative analysis)	RO bathymetric chart (quantitative analysis)

bathymetry calculated for each one of these images was also compared in a quantitative way with those provided by the Oceanographic Observatory of the Iberian Margin (the local RO measurements). The results also reveal average bathymetric differences that range from about a few decimetres to some meters. A combined solution that merges the results of all the image set slight improves the results when compared with the RO chart. The 20 m calculated isobaths provided the best performance while the 30 m calculated isobaths provided the lowest performance in this comparison. The relative error of the water depth ranges between 6% and 10%. The present methodology has proven to give more accurate results than those derived from a single image, given the uncertainty in the λ and λ_0 estimations.

Several factors can be suggested to justify the discrepancies between the obtained results and they can be divided into two groups: (i) internal factors related with the methodological approach (FFT cell size, cell shift and mode of implementation); (ii) internal factors related with the adopted variables used to derive water depth (D) from a particular FFT cell through the linear dispersion relation (offshore wave parameters calculated from a SAR image as wavelength and period or measured wave parameters from an offshore local wave bouy); (iii) external factors as the intensity of the swell waves, relation between swell and sea waves. The diversity of factors and complexity of the analysis justify additional work.

Acknowledgments

References

Adler-Golden, S.M., Acharya, P.K., Berk, A., Matthew, M.W., Gorodetzky, D., 2005. Remote bathymetry of the littoral zone from AVIRIS, LASH, and QuickBird imagery. IEEE Trans. Geosci. Remote Sens. 43 (2), 337–347.

Andrade, C., Freitas, M.C., 2002. Coastal zones. In: Santos, F.D., Forbes, K., Moita, R. (Eds.), Climate Changes in Portugal - Scenarios, Impacts and Adaptation Measures. SIAM Project. Gradiva, Lisbon (456 p).

Baptista, P., Cunha, T.R., Bernardes, C., Gama, C., Ferreira, Ó., Dias, A., 2011. A precise and efficient methodology to analyse the shoreline displacement rate. J. Coast. Res. 27 (2), 223–232.

Basu, A., Malhotra, S., 2002. Error detection of bathymetry data by visualization using GIS. ICES J. Mar. Sci. 59, 226–234.

Bell, P., 1999. Shallow water bathymetry derived from an analysis of X-band marine radar images of waves. Coast. Eng. 37, 513–525.

Birkemeier, W.A., 1985. Time scales of nearshore profile change. In: Proc. 19th International Conference on Coastal Engineering. ASCE, New York, pp. 1507–1521.

Brusch, S., Held, P., Lehner, S., Rosenthal, W., Pleskachevsky, A., 2011. Underwater bottom topography in coastal areas from TerraSAR-X data. Int. J. Remote Sens. 32 (16), 4527–4543.

Cea, L., French, J.R., 2012. Bathymetric error estimation for the calibration and validation of estuarine hydrodynamic models. Estuar. Coast. Shelf Sci. 100, 124–132.

Dai, Z., Liu, J.T., Fu, G., Xie, H., 2013. A thirteen-year record of bathymetric changes in the North Passage, Changjiang (Yangtze) estuary. Geomorphology 187, 101–107.

EL-Hattab, A.I., 2014. Single beam bathymetric data modelling techniques for accurate maintenance dredging. Egypt. J. Remote Sens. Space. Sci. 17, 189–195.

Ferreira, Ó., 1993. Caracterização dos Principais Factores Condicionantes do Balanço Sedimentar e da Evolução da Linha de Costa Entre Aveiro e o Cabo Mondego. MSc Thesis. University of Lisbon (166 p).

Finkl, C.W., Benedet, L., Andrews, J.L., 2005. Interpretation of seabed geomorphology based on spatial analysis of high-density airborne laser bathymetry. J. Coast. Res. 21 (3), 501–514.

Goto, K., Takahashi, J., Oie, T., Imamura, F., 2011. Remarkable bathymetric change in the nearshore zone by the 2004 Indian Ocean tsunami: Kirinda Harbor, Sri Lanka. Geomorphology 127 (1–2), 107–116.

Grifoll, M., Jordà, G., Espino, M., Romo, J., García-Sotillo, M., 2011. A management system for accidental water pollution risk in a harbour: the Barcelona case study. J. Mar. Syst. 88, 60–73.

Horstmann, J., Borge, J., Seemann, J., Carrasco, R., Lund, B., 2015. Chapter 16 - wind, wave, and current retrieval utilizing X-band marine radars. In: Liu, Yonggang, Kerkering, Heather, Weisberg, Robert H. (Eds.), Coastal Ocean Observing Systems. Academic Press, pp. 281–304.

Lehner, S., Pleskachevsky, A., Bruck, M., 2012. High-resolution satellite measurements of coastal wind field and sea state. Int. J. Remote Sens. 33 (23), 7337–7360.

Li, X., Lehner, S., Rosenthal, W., 2010. Investigation of ocean surface wave refraction using TerraSAR-X data. IEEE Trans. Geosci. Remote Sens. 48 (2), 830–840.

Lippmann, T.C., Holman, R.A., 1990. The spatial and temporal variability of sand bar morphology. J. Geophys. Res. 95, 11575–11590.

Lippmann, T.C., Holman, R.A., Hathaway, K.K., 1993. Episodic, non-stationary behavior of a two sand bar system at Duck, NC, USA. J. Coast. Res. SI, 49–75.

Lopes, C.L., 2016. Flood Risk Assessment in Ria de Aveiro Under Present and Future Scenarios. Ph.D. Thesis. University of Aveiro (225pp).

Losi, V., Ferrero, T.J., Moreno, M., Gaozza, L., Rovere, A., Firpo, M., Marques, J.C., Albertelli, G., 2013. The use of nematodes in assessing ecological conditions in shallow waters surrounding a Mediterranean harbour facility. Estuar. Coast. Shelf Sci. 130, 209–221.

Matsuyama, M., Walsh, J.P., Yeh, H., 1999. The effect of bathymetry on tsunami characteristics at Sisano Lagoon, Papua New Guinea. Geophys. Res. Lett. 26 (23), 3513–3516.

Mishra, M.K., Ganguly, D., Chauhan, P., Ajai, 2014. Estimation of coastal bathymetry using RISAT-1 C-band microwave SAR data. IEEE Geosci. Remote Sens. Lett. 11 (3), 671–675.

Nishida, T., Mohri, M., Itoh, K., Nakagome, J., 2001. Study of bathymetry effects on the nominal hooking rates of yellowfin tuna (*Thunnus albacares*) and bigeye tuna (*Thunnus obesus*) exploited by the Japanese tuna longline fisheries in the Indian Ocean. In: Indian Ocean Tuna Commission Proceedings. 4. pp. 191–206.

Patgaonkar, R.S., Ilangovan, D., Vethamony, P., Babu, M.T., Jayakumar, S., Rajagopal, M.D., 2007. Stability of a sand spit due to dredging in an adjacent creek. Ocean Eng. 34, 638–643.

Phillips, O.M., 1977. The Dynamics of the Upper Ocean, 2nd ed. Cambridge University Press.

Plant, N.G., Holman, R.A., Freilich, M.H., Birkemeier, W.A., 1999. A simple model for interannual sandbar behavior. J. Geophys. Res. 104, 15755–15776.

Plant, N., Holland, k.T., Puleo, J.A., 2002. Analysis of the scale of errors in nearshore bathymetric data. Mar. Geol. 191, 71–86.

Pleskachevsky, A., Lehner, S., Heege, T., Mott, T., 2011. Synergy and fusion of optical and synthetic aperture radar satellite data for underwater topography estimation in coastal areas. Ocean Dyn. 61 (12), 2099–2120.

Ranasinghe, P.L., Goto, K., Takahashi, T., Takahashi, J., Wijetunge, J.J., Nishihata, T., Imamura, F., 2013. Numerical assessment of bathymetric changes caused by the 2004 Indian Ocean tsunami at Kirinda Fishery Harbor, Sri Lanka. Coast. Eng. 81, 67–81.

Ridente, D., Martorelli, E., Bosman, A., Chiocci, F.L., 2014. High-resolution morpho-bathymetric imaging of the Messina Strait (Southern Italy). New insights on the 1908 earthquake and tsunami. Geomorphology 208, 149–159.

Ruessink, B.G., Kroon, A., 1994. The behavior of a multiple bar system in the nearshore zone of Terschelling, the Netherlands, 1965–1993. Mar. Geol. 121, 187–197.

Sandidge, J.C., Holyer, R.J., 1998. Coastal bathymetry from hyperspectral observations of water radiance. Remote Sens. Environ. 65 (3), 341–352.

Sentinel-1 Team, 2013. Sentinel-1 Handbook. (GMES-S1OP-EOPG-TN-13-0001).

Vitorino, J., Oliveira, A., Jouanneau, J., Drago, T., 2002. Winter dynamics on the northern Portuguese shelf. Part 1: physical processes. Prog. Oceanogr. 52, 129–153.

Wiehle, S., Pleskachevsky, A., 2018. Bathymetry derived from Sentinel-1 Synthetic Aperture Radar data. In: 12th European Conference on Synthetic Aperture Radar Electronic Proceedings. Verband der Elektrotechnik Elektronik Informationstechnik e.V. Kartonhülle, Aachen, Germany, 978-3-8007-4636-1, pp. 1489.

Winant, C.D., Inman, D.L., Nordstrom, C.E., 1975. Description of seasonal beach changes using empirical eigenfunctions. J. Geophys. Res. 80, 1979–1986.

Young, I.R., Rosenthal, W., Ziemer, F., 1985. A three-dimensional analysis of marine radar images for the determination of ocean wave directionality and surface currents. J. Geophys. Res. 90_C1, 1049–1059.